Biomaterials 255 (2020) 120186

Contents lists available at ScienceDirect

Biomaterials

journal homepage: www.elsevier.com/locate/biomaterials

Albumin-constrained large-scale synthesis of renal clearable ferrous sulfide quantum dots for T_1-Weighted MR imaging and phototheranostics of tumors

Weitao Yang[a,1], Chenyang Xiang[a,1], Yan Xu[a], Shizhen Chen[b], Weiwei Zeng[a], Kai Liu[a], Xiao Jin[a], Xin Zhou[b,**], Bingbo Zhang[a,*]

[a] Department of Medical Ultrasound, Shanghai Tenth People's Hospital, Tongji University Cancer Center, Tongji University School of Medicine, Shanghai, 200072, China
[b] Key Laboratory of Magnetic Resonance in Biological Systems, State Key Laboratory of Magnetic Resonance and Atomic and Molecular Physics, National Center for Magnetic Resonance in Wuhan, Wuhan Institute of Physics and Mathematics, Innovation Academy for Precision Measurement Science and Technology, Chinese Academy of Sciences, Wuhan, 430071, China

ARTICLE INFO

Keywords:
Biomimetic synthesis
T_1-weighted MR imaging
Ferrous sulfide
Renal metabolism
Phototheranostics

ABSTRACT

Ultrasmall-sized iron-based nanoparticles are showing increasing potentials to be alternatives as T_1-weighted magnetic resonance imaging (MRI) contrast agents to the currently-used gadolinium-based compounds. However, their synthesis particularly in a large-scale and green fashion is still a big challenge. Herein, we report an albumin-constrained strategy to synthesize tiny and highly dispersible ferrous sulfide (termed FeS@BSA) quantum dots (QDs) at ambient conditions. FeS@BSA QDs exhibit ultrasmall size of *ca.* 3.0 nm with an ultralow magnetization, affording them an appealing longitudinal relaxivity for T_1-weighted MRI. The design principle leverages on albumin-mediated biomimetic synthesis and spatial isolation of the protein interface prevents bulk aggregation of the particles. Albumin was found to play crucial roles in the synthesis process: a constrained-microenvironment reactor for particle growth, a water-soluble layer for colloidal stability and a carrier for multi-functionality. This synthetic strategy was found facile, green and particularly large-scalable to 10 L. Mice experiments show good T_1-weighted MRI capability of FeS@BSA QDs, significantly lighting the whole body organs, blood vessels and tumors. And interestingly, these QDs can be further used to conduct phototheranostic of tumor benefited from their intense absorption at near-infrared region. In particular, they can be cleared *via* glomerular filtration into bladder after treatment. Given this approach is biomimetic, scalable and does not require any complicated chemical synthesis or modifications, the method demonstrated here will find great potentials for clinical translation in T_1-weighted MRI of diseases and inspire other functional tiny nanoprobes for biomedical applications.

1. Introduction

Magnetic resonance (MR), as an established powerful imaging modality, has been widely used in clinics for tumor diagnosis [1]. It is not only safe and noninvasive without use of any radiotracers but also provides tomography information on live organisms without penetration limitations [2,3]. Usually, MR contrast agents (CAs) are highly needed to identify details of tumor for exploring extra molecular information which is not acquired by plain imaging [4–7].

In general, two main categories of MR CAs are used in clinics to increase MR enhancement/sensitivity for accurate early diagnosis of tumors or other diseases, namely the Gd-based compounds or nanostructures and iron-based nanostructures. The former usually acts as T_1-weighted MR imaging CAs and has served in clinics for decades; however, Gd ions degraded or leaked from the injected matrix are frequently reported to be highly toxic in human body, especially prone to cause nephrogenic systemic fibrosis (NSF) [8]. By comparison, iron-based MR CAs are considered to be biocompatible since their main composition is iron which is indispensable in human body [9]. In 1996, food and drug administration (FDA) approved ferumoxides (iron oxide nanoparticles) as MR CAs for liver disease diagnosis [10]. Nevertheless, most of iron-based nanoparticles including ferumoxides are T_2-weighted MR imaging CAs because of its oversize. They produce dark signals in lesions which are easily disturbed by other hypointense

* Corresponding author.
** Corresponding author.
E-mail addresses: xinzhou@wipm.ac.cn (X. Zhou), bingbozhang@tongji.edu.cn (B. Zhang).
[1] These authors contributed equally to this study.

https://doi.org/10.1016/j.biomaterials.2020.120186
Received 1 March 2020; Received in revised form 3 June 2020; Accepted 8 June 2020
Available online 16 June 2020
0142-9612/

regions such as calcification, air, blood clots, and haemorrhage. Therefore, developing ultrasmall-sized iron-based nanoparticles for T_1 positive imaging is of great importance in MR diagnosis.

Ultrasmall-sized iron-based nanoparticles are showing increasing potentials to be alternatives as T_1-weighted positive MR CAs to the currently-used gadolinium-based compounds, and relevant research including synthesis of iron-based compounds/nanoparticles, surface engineering, and imaging performance assessment has been a hot topic worldwide [11]. In recent years, ultrasmall-sized iron oxide nanoparticles have been synthesized by a few methods and they showed good performance on producing T_1-weighted MR signals due to low magnetization by a strong size-related surface spin-canting effect [12–15]. Ling et al. [16] synthesized small-sized iron oxide nanoclusters *via* "heat up" method and confirmed they exhibited significantly improved biosafety and a much lower risk of causing NSF than Gd-based CAs. According to a similar method, Lu et al. [17] synthesized uniform 2 nm iron oxide nanoclusters for *in vivo* T_1-weighted MR imaging in large animal models, including beagle dogs and macaques, and they evaluated their potential toxicity. While these iron oxide nanostructures are effective as T_1 MR CAs, their MR relaxivity needs to be improved and more importantly, other iron materials and their synthetic methodology should be explored.

In contrast, FeS nanoparticles not only possess MR imaging capability but also exhibit higher absorbance in near infrared region (NIR), and can convert the absorbed NIR light into heat [18]. Thus, it is able to be served as MR/PA bimodal imaging CAs for tumor diagnosis and then guide tumor photothermal therapy (PTT). In the previous studies, some strategies have been proposed to synthesize FeS nanoparticles, such as hot-injection and hydrothermal method [19–21]. Although by using these methods we can fabricate FeS nanoparticles, they are involving with harsh reaction conditions, such as inert gas shielding, high temperature, and toxic organic solvents. And worse of all, the sizes of the obtained FeS nanoparticles are usually too large and thus only can be used for T_2-weighted MR imaging. Moreover, it is difficult to be cleared by kidneys, resulting in adverse effects due to iron retention in liver, which is not preferred by radiologist. Therefore, developing a green method to synthesize extremely small-sized and renal-clearable FeS QDs for T_1-weighted MR/PA imaging and tumor PTT is highly desired.

In this study, protein-mediated biomimetic strategy is employed since this synthetic approach is green chemistry without using any organic solvents and is conducted at physiological temperature [22]. And particularly, we found protein-mediated synthesis was inclined to produce small nanoparticles in our previous work [23–26]. Inspired by these, we try to use albumin and its constrained and delimited effects to synthesize extremely small-sized FeS QDs. Results show these QDs have a small size and good longitudinal relaxivity, excellent photothermal conversion effect, and renal clearance characteristic. Thus, it can be used for *in vivo* T_1-weighted MR/PA bimodal imaging-guided tumor PTT, and particularly, after imaging and therapy applications, these QDs can be cleared from body *via* urine. The synthesis process and application are illustrated in Scheme 1.

2. Materials and methods

2.1. Materials

Bovine serum albumin (BSA), $FeCl_2{\cdot}4H_2O$ ($\geq$99.0%), sodium sulfide nonahydrate ($Na_2S{\cdot}9H_2O$), and sodium hydroxide (NaOH) were ordered from Sigma-Aldrich. Phosphate Buffered Saline (PBS) was ordered from Aladdin. Cell Counting Kit-8 (CCK-8) was purchased from KeyGEN bioTECH (KGA317, Nanjing, China). Paraformaldehyde (4%) was purchased from Solarbio Life Science. All the reagents were analytical grade and used without purification.

2.2. Synthesis of FeS@BSA QDs

The FeS@BSA QDs were synthesized following a BSA-constrained biomimetic method [23]. Typically, 200 mg of BSA was dissolved in 8 mL of purified water followed by addition of $FeCl_2{\cdot}4H_2O$ solution (0.1 M, 1 mL). Then, the mixture was stirred at 37 °C for 3 min and a stock solution of NaOH (1 M, 0.5 mL) was introduced to adjust the pH of solution to be 11. Then, an aqueous solution of $Na_2S{\cdot}9H_2O$ (1 mL, 0.8 M) was injected into the mixture. After 3 h of stirring at 37 °C, the deep green mixture was collected and purified by dialyzing for 24 h against water.

2.3. Materials characizations

The morphology and size of FeS@BSA QDs were observed by transmission electron microscopy (TEM). The UV–vis absorption spectrum and hydrodynamic size of FeS@BSA QDs were measured by Zetasizer (Nano-ZS90, Malvern) and ultraviolet–visible spectrophotometer (Cary 60, Agilent), respectively. The element composition and valence state of FeS@BSA QDs were analyzed by X-ray photoelectron spectroscopy (XPS) (*1/AXIS UltraDLD, Kratos, Japan). The Fe concentration was determined by inductively coupled plasma atomic emission spectrometer (ICP-AES, 167 nm–785 nm/725, Agilent, USA).

2.4. Relaxivity (r_1) and in vitro MR phantom imaging

The longitudinal time (T_1) of FeS@BSA QDs at different concentration were obtained by using a MR Analyzer (Bruker, Minispec mq 60). Then, the linear fitting curve of Fe concentration (mM) *versus* $1/T_1$ (s^{-1}) were obtained, and the corresponding slop is longitudinal relaxivity (r_1).

For *in vitro* phantom, T_1-weighted MR experiments, different concentration of FeS@BSA QDs were prepared, and the corresponding T_1-weighted MR images was taken on Ingenia 3.0 T MR scanner (PHILIPS) according to the following parameters: NS = 2, slice width = 5.0 mm, slice gap = 0.55 mm, slices = 8, TR/TE = 500 ms/18.2 ms, FOV = 80 mm × 80 mm, matrix acquisition = 90 × 90.

2.5. In vitro photothermal conversion and photoacoustic imaging

Different concentrations of FeS@BSA QDs solution were irradiated for 5 min by 660 nm laser (2 W/cm^2). The real-time temperature of all samples was measured and recorded by a thermal camera every minute. The pure water was irradiated under the same conditions, which is served as a control group. Furthermore, to evaluate the photothermal stability of FeS@BSA QDs, Photothermal cycling test was performed repeatedly to detect the temperature increase after laser irradiation. The hydrodynamic size of FeS@BSA QDs was measured before and at 4 h, 24 h, and 7 days post-irradiation.

In vitro PA imaging was conducted on a Vevo LAZR Imaging System (FujiFilm VisualSonics Inc.). Firstly, different wavelength of excitation light was used to collect the optimized photoacoustic signals. The phantoms with different concentrations of FeS@BSA QDs (0.3, 0.6, and 1.2 mg/mL) solution were placed in the PA imaging system and scanned to collect the PA images and the corresponding PA signals.

2.6. Cytotoxicity study

The *in vitro* cytotoxicity of FeS@BSA QDs was determined by detecting the 4T1 cell viabilities after incubation with FeS@BSA QDs using a standard CCK-8 assay. In brief, 4T1 cells were seeded into 96-well plates followed by cultivation for 24 h to allow cells to attach to the surface. Then, the medium was discarded, and the fresh medium containing various concentrations of FeS@BSA QDs (50, 100, 250, 500 and 1000 μg/mL) were added into the plates. After another 24 or 48 h of incubation at 37 °C, the supernatant was discarded, and the cells

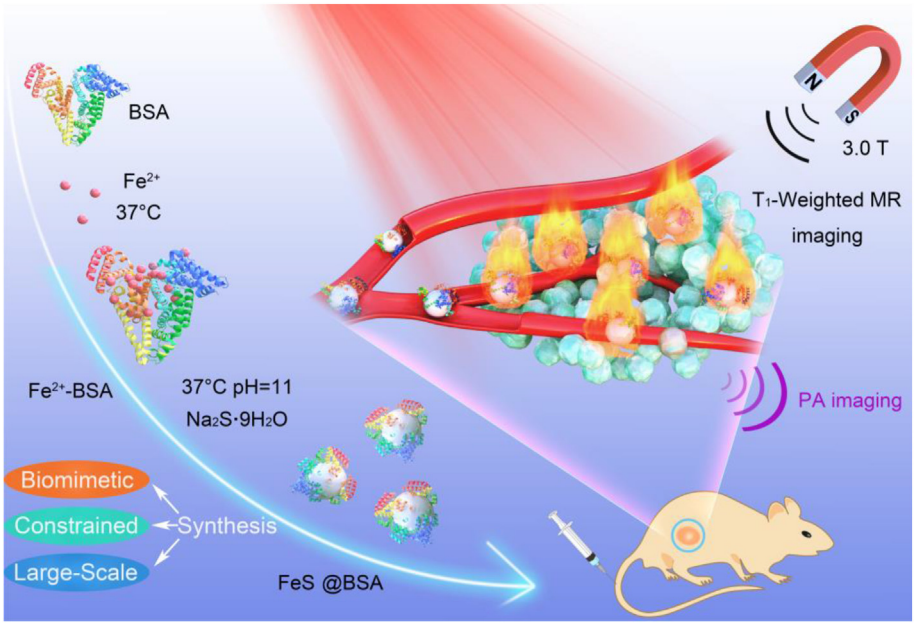

Scheme 1. Schematic illustration of albumin-constrained biomimetic synthesis of ultrasmall-sized FeS@BSA QDs for *in vivo* T_1-weighted MR imaging and phototheranostics of tumors.

were rinsed three times with PBS, followed by addition of CCK-8 solution (10 μL). Then, after 2 h of incubation, absorbance value at 450 nm was measured by using a microplate reader. The cell viability was obtained by calculating the OD value ratio of FeS@BSA QDs treatment group and control group. The cytotoxicity of FeS@BSA QDs to normal cells (DC 2.4) cells was investigated according to the similar procedure.

To investigate the photothermal conversion effect of FeS@BSA QDs on tumor cells inhibition, 4T1 cells were divided into control group, laser irradiation group (1 W/cm^2, 5 min), FeS@BSA QDs treatment group (500 μg/mL), and FeS@BSA QDs (500 μg/mL) plus laser irradiation group (5 min, 1 W/cm^2). The corresponding cell viabilities of four groups were measured according to the abovementioned CCK8 assay.

2.7. *In vivo* T_1-weighted MR/PA/fluorescence imaging

All animal experiments were conducted in compliance with a standard guideline approved by the Institutional Animal Care and Use Committee of Tongji University. The 4T1 tumor models were generated by subcutaneous injection of 1×10^6 cells suspended in 100 μL of PBS into the right thigh of mice (6 weeks old, female).

In vivo MR imaging of tumor, liver, bladder, and blood vessel: balb/c mice were anesthetized through intraperitoneal injection of pentobarbital sodium (100 μL, 1%), and then scanned on clinical MR imaging system (PHILIPS, 3.0 T) to obtain pre-injection MR image of kidney, bladder, tumor, liver, and blood vessel. Then, the mice were injected with 150 μL of FeS@BSA QDs solution through tail vein. Then, MR images at 1 h, 2 h, 3 h, and 5 h post-injection were acquired. The MR sequences were set as follows: FOV read = 90 mm, TR/TE = 600/20, slice gap = 0.5 mm, FOV phase = 90 mm, ST = 1.2, slice pos = 12.9, slice width = 3.5 mm, flip angle = 90°.

For *in vivo* tumor PA imaging, balb/c mice were anesthetized through intraperitoneal injection of pentobarbital sodium (100 μL, 1%), followed by irradiation with pulsed laser and collection the pre-injection image on PA imaging system (FujiFilm VisualSonics Inc.). Subsequently, the mice were intravenously injected with FeS@BSA QDs solution. Then, PA images of tumor at 1 h, 2 h, 3 h, and 5 h post-injection were obtained at an excitation wavelength of 680 nm.

2.8. *In vivo tumor photothermal therapy*

4T1 tumor-bearing balb/c mice were divided into 4 groups (3 mice in each group): Group 1 was intravenously administered with PBS as the control group; Group 2 was irradiated by laser only; Group 3 was administered injected with FeS@BSA QDs only; Group 4 was intravenous injected with FeS@BSA QDs followed by laser irradiation (660 nm, 2 W/cm^2) at 5 h post-injection; The tumor temperature of mice in group 2 and group 4 was monitored by using a thermal camera. The tumor volumes and body weights of all mice were measured and recorded every day. Tumor volume was calculated according to the equation: $V = (W^2 \times L)/2$, where W and L represent the shortest and longest diameters of tumor. At 15 d post-treatment, the mice were sacrificed, and the tumors were collected for H&E staining analysis.

2.9. *In vivo toxicity evaluation*

Twelve balb/c mice (6–7 weeks, Female) were divided into 3 groups (n = 4 per group), followed by injection of PBS (group 1) and FeS@BSA QDs (group 2 and 3, doge: 20 mg/kg mice) through tail vein, respectively. Then, the mice were anaesthetized at day 1 and day 14 post-injection, and the blood samples were collected for biochemistry (serum) and blood routine (whole blood) analysis. At the same time, the spleen, heart, kidney, liver, and lung tissues were harvested and rinsed three times with PBS, followed by immobilization in formalin. Then, all tissues were embedded in paraffin and sectioned at 3-μm thickness, followed by H&E staining and finally observed under a microscope.

3. Results and discussion

3.1. *Synthesis and characterizations of FeS@BSA QDs*

Ultrasmall-sized FeS@BSA QDs were synthesized through a green and facile protein-biomimetic strategy, which is illustrated in Scheme 1. The synthesis process of FeS@BSA QDs can be divided into three steps: Firstly, Fe^{2+} was intensely anchored by BSA depending on the strong affinity of metal ions with carboxyl groups, forming Fe^{2+}-BSA complex; Secondly, NaOH solution was added to produce $Fe(OH)_2$ intermediates and adjust the pH of solution to strong alkaline (~11), making the conformational transformation of BSA from a 3D folding structure into

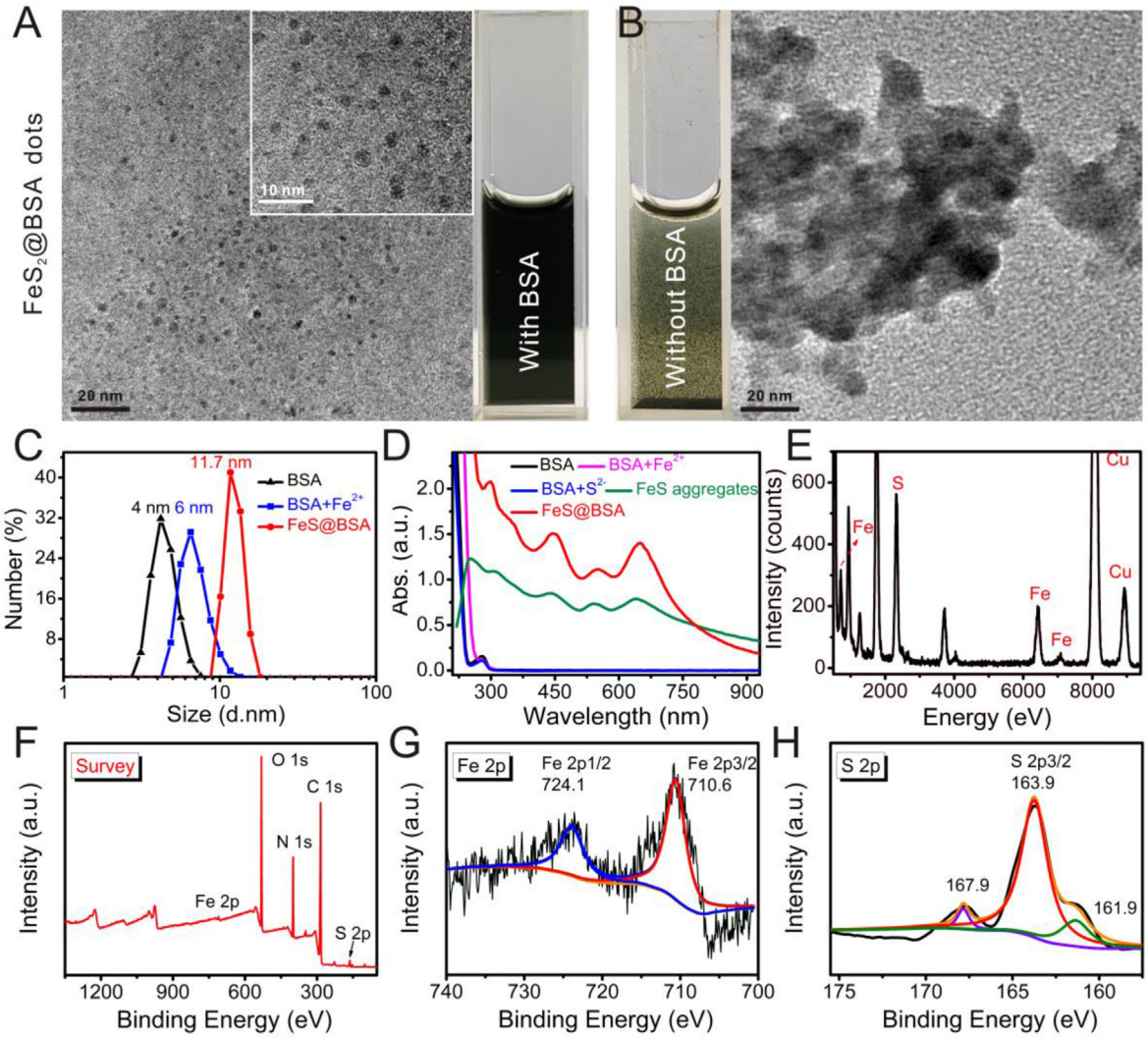

Fig. 1. Characterizations of FeS@BSA QDs. Representative TEM (scale bar: 20 nm), HRTEM image (the inset, scale bar: 10 nm), and a digital picture of FeS synthesized (A) with and (B) without BSA. (C) The hydrodynamic size of BSA, BSA + Fe^{2+}, and FeS@BSA QDs. (D) UV–vis absorption spectra of BSA, BSA + Fe^{2+}, BSA + S^{2+}, FeS aggregates, and FeS@BSA QDs. (E) EDS and (F) XPS survey spectrum of FeS@BSA QDs, (G) Fe 2p, and (H) S 2p XPS spectra, and their corresponding fitting curves.

an unfolded configuration; Finally, $Na_2S{\cdot}9H_2O$ was added and FeS@BSA QDs were obtained based on a co-precipitation reaction. This one-pot synthesis was extremely convenient, environmentally benign, and reproducible for large-scale preparation. In this study, we found this reaction can be scaled up to 10 L and even more (Fig. S1). The physical and chemical properties of the resultant FeS@BSA QDs were studied. A representative TEM image in Fig. 1A shows uniform, good monodispersity and ultrasmall size (~3 nm) of the synthesized FeS@BSA QDs due to the constrained effect of BSA inhibiting the overgrowth of particles in reaction. Moreover, the protein coating on QDs can delimit each other from aggregation.

In order to show the indispensable role of BSA in this process, we tried to synthesize FeS without using BSA, but unfortunately, we just obtained large-sized aggregates in the solution (Fig. 1B). In contrast, BSA-constrained synthesized FeS@BSA QDs were found to be very small and dispersed well in the solution. As displayed in Fig. 1C, the average hydrodynamic size (HD) of FeS@BSA QDs was measured to be 11.7 nm with a good polydispersity index (PDI = 0.195) and no large aggregates. Thus, it can be concluded that BSA played roles of constrained-reaction site provider and stabilizer that can limit the particle further growth and avoid large aggregates formation. According to previous reports, an ultrasmall size of ferrous nanoparticles is a prerequisite for T_1-weighted MR imaging and *in vivo* kidney clearance [13,27]. In addition, the zeta potential of FeS@BSA QDs was −19.2 mV due to the presence of carboxyl groups in BSA.

During the synthesis process, HD and absorption spectra were monitored. As displayed in Fig. 1C and D, HD was increased from 4 nm (pure BSA) to 6 nm (Fe^{2+}-BSA complex) and finally to 11.7 nm. And interestingly, the pattern of UV–vis absorption spectrum of FeS@BSA QDs were found pretty like that of semiconductor CdSe quantum dots [28]. We also found the characteristic absorption peak at 650 nm appears both in the sample of FeS aggregates and FeS@BSA QDs, but the absorption peak of FeS@BSA QDs is much sharper than that of FeS aggregates, which is attributed to the delimited distribution of FeS@BSA QDs in solution. The synthesis conditions were optimized by changing the molar ratio of Fe/S, reaction time, reaction temperature, and BSA amount. As shown in Figs. S2A–S2F, with the increase of reaction time and the decrease of Fe/S molar ratio from 2/1 to 1/16, the characteristic absorption peaks at 650 nm become more and more obvious. Reaction temperature and the used BSA amount were found to be critical in controlling size (Figs. S3 and S4). It can be seen that high temperature leads to large size and abundant albumin should be guaranteed in the reaction to provide constraining effect for limiting particle growth. By comparing their absorbance value at 650 nm and

HD (Figs. S2–S4), the appropriate Fe/S molar ratio, reaction time, and temperature for reaction were found to be 1/8, 3 h, and 37 °C, respectively.

To determine the elemental composition and chemical valence of FeS@BSA QDs, energy dispersive spectrum (EDS) and X-ray photoelectron spectroscopy (XPS) studies were conducted. As depicted in Fig. 1E and F, EDS shows co-existence of Fe and S elements in the as-prepared sample, which is also confirmed by XPS survey spectra. Fe (2p) and S (2p) peaks were analyzed with XPS Peak 4.1 software to confirm their definite chemical states in the formed FeS@BSA QDs. Fig. 1G shows the Fe (2p3/2) binding energy of 710.6 eV is characteristic peak of FeS, with a Fe (2p1/2) binding energy of 724.1 eV [29,30]. For sulfur peaks, the S (2p3/2) binding energy of 163.9 eV also confirms the presence of FeS. Additionally, a binding energy of 161.9 eV is associated with S^{2-}. The feeble peak at 167.9 eV could be attributed to the organic sulfur species from BSA (Fig. 1H) [31]. X-ray diffraction analysis (XRD) was further used to study the crystal phase of the resultant FeS@BSA QDs (Fig. S5). It shows the diffraction peaks around at 2-Theta = 17.618°, 30.063°, and 34.46° that correspond to the (001), (101), and (111) planes, respectively, which attributes to the mackinawite FeS (PDF#15–0037).

3.2. *In vitro* MR/PA imaging and photothermal conversion capability study

The longitudinal (r_1) relaxivity was measured to examine the feasibility of using FeS@BSA QDs as T_1 MR CAs. As displayed in Fig. 2A, the r_1 was measured to be 5.35 $mM^{-1}s^{-1}$, which is higher than that of the clinically-used MR CAs (Gd-diethylenetetramine pentaacetic acid (Gd-DTPA), r_1 = 3.1 $mM^{-1}s^{-1}$) [32] and the previously reported iron-based T_1 MR CAs (Fe-CPNDs, r_1 = 1.5 $mM^{-1}s^{-1}$ [33]; PEG–IONCs, r_1 = 3.91 $mM^{-1}s^{-1}$ [17]; FeS-PEG, r_1 = 0.34 $mM^{-1}s^{-1}$ [31]). In addition, we found the r_1 of FeS@BSA QDs was much higher than that of FeS aggregates (r_1 = 0.2 $mM^{-1}s^{-1}$). Large-sized FeS nanoparticles or its bulk counterparts are reported as T_2 MR CAs due to their enhanced ordered spins induced large magnetization [13]. In this study, we used the constrained and delimited effects of albumin to inhibit the growth and aggregation of FeS nanoparticles, resulting in an ultrasmall size and highly dispersion of sample. These features therefore provide a relatively lower magnetization (Fig. S6) and a higher longitudinal relaxivity. It should be pointed out here that the magnetization of materials (such as large-sized iron oxide nanoparticles) affects the static magnetic field of MRI equipment, which usually results in darkening or quenching the signals when performing MR imaging [34]. Thus, to reduce this effect, small or ultrasmall-sized particles are preferred since they possess very low magnetizations. Moreover, the protein layer of albumin allows good dispersion state of nanoparticles and particularly prolongs rotational correlation time (τ_R) and also enhances sufficient water-metal interactions (q). These factors collectively improve the r_1 of FeS@BSA QDs [35–38]. The T_1-weighted MR imaging capability of FeS@BSA QDs was further assessed and found to be concentration-

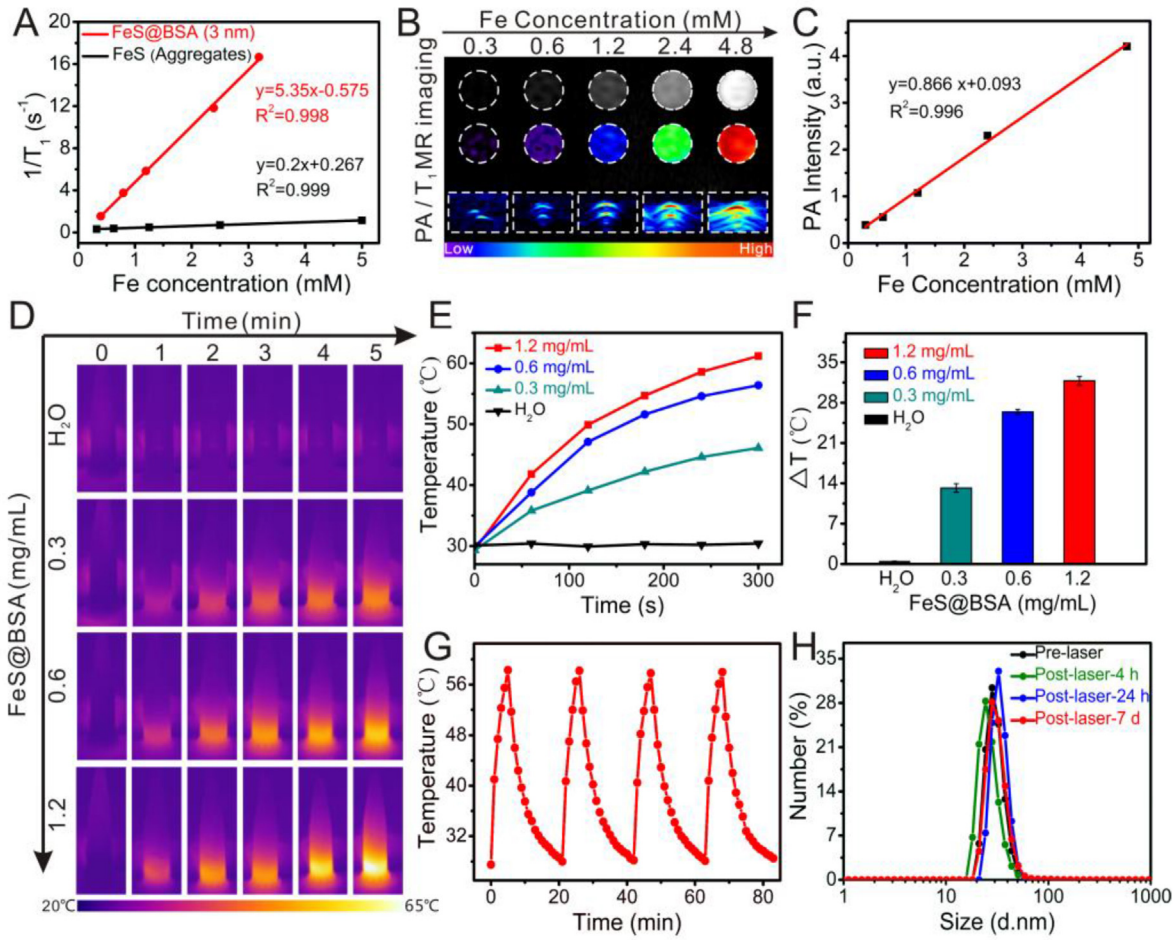

Fig. 2. *In vitro* MR/PA imaging and photothermal conversion capabilities of FeS@BSA QDs. (A) The longitudinal relaxation rate (r_1), (B) *in vitro* concentration-dependent T_1-weighted MR images, and PA images of FeS@BSA QDs; (C) The linear fitting curve between PA signal intensity and Fe concentration; (D) Time (0 min–5 min) and concentration (0.3–1.2 mg/mL)-dependent infrared thermal images of FeS@BSA QDs before and after laser irradiation (660 nm, 2 W/cm^2). (E) The corresponding temperature increment curve and (F) temperature increase (ΔT) *versus* FeS@BSA concentration; (G) Photothermal conversion recycling profiles of FeS@BSA QDs after laser irradiation for four laser ON/OFF cycles; H) The HD change of FeS@BSA QDs before and at 4 h, 24 h, and 7 days post laser irradiation.

dependent in generating gradient brightening signals (Fig. 2B), demonstrating FeS@BSA QDs are able to serve as a new kind of highly efficient T_1 MR CAs. Then, the colloidal stability of FeS@BSA QDs was evaluated by monitoring time-dependent UV–*vis* absorption spectrum and longitudinal relaxation time (T_1). As shown in Fig. S7, after 24 h, the absorption peak position, absorption intensity, and T_1 displayed negligible change, which indicate good colloidal stability of FeS@BSA QDs due to the strong encapsulation of albumin for nanoparticles.

Interestingly, compared with other iron-based materials, FeS@BSA QDs were found to have a specific and strong absorption in the near-infrared region. Leveraging this property, we found FeS@BSA QDs can convert the absorbed light energy to heat. As displayed in Fig. 2B, after pulsed laser irradiation, the PA signal of FeS@BSA solution gradually becomes more and more stronger with the increase of concentration, and it displays a good linear relationship (R^2 = 0.996, Fig. 2C). As such, besides being MR CAs, FeS@BSA QDs can also serve as PA CAs to achieve ultrasensitive tumor imaging.

Subsequently, the photothermal conversion capability and photostability of FeS@BSA QDs were characterized. As depicted in infrared thermal images (Fig. 2D) and temperature increase curve (Fig. 2E), the temperature of FeS@BSA solution rapidly increases after laser irradiation for 5 min in a concentration-dependent manner, and the maximum change of FeS@BSA (0.3, 0.6, and 1.2 mg/mL) in temperature (ΔT_{max}) reaches 13.2 °C, 26.4 °C, and 31.8 °C, respectively (Fig. 2F). Under the same conditions, no significant change was observed (ΔT_{max} = 0.5 °C) for an equal volume of pure water. According to previously reported method [39,40], the photothermal conversion efficiency of FeS@BSA QDs was calculated to be 30.04% (Fig. S8). Furthermore, it was found this photothermal conversion effect is very stable (Fig. 2G), even after performing four cycles of ON/OFF laser irradiations (5 min ON and 15 min OFF). The colloidal stability of FeS@BSA QDs after irradiation was found good, which is evaluated by DLS study. The HD is in the range of 11 nm–15 nm without aggregations (Fig. 2H). These results indicate the good stability of FeS@BSA QDs during photothermal conversion.

3.3. In vitro cytotoxicity, cellular uptake, and phototherapy study

To investigate the cytotoxicity of FeS@BSA QDs, CCK-8 assays were carried out on normal cells (DC 2.4) and 4T1 breast cancer cells, respectively. Different concentrations (50 μg/mL, 100 μg/mL, 250 μg/mL, 500 μg/mL, and 1000 μg/mL) of FeS@BSA QDs were prepared, followed by incubation with DC 2.4 and 4T1 cells, respectively. As presented in Fig. 3A and B, after 24 h and 48 h of incubation, the viabilities of these two kinds of cells can exceed 80% even at 1000 μg/mL, indicating the good biocompatibility of FeS@BSA QDs, which is mainly attribute to the non-toxic element use and the surface encapsulation of albumin.

Subsequently, to study the cellular uptake behavior of FeS@BSA QDs, a typical hydrophobic and efficient fluorescence squaraine (Sq) dye (fluorescence emission peak: 685 nm, Fig. S9), was pre-assembled on FeS@BSA QDs based on hydrophobic-hydrophobic binding force, forming FeS@BSA:Sq nanoprobes, which is confirmed by noticing a newly emerged 668 nm absorption peak on FeS@BSA:Sq structure, compared with that of pure Sq (Fig. 3C). As displayed in confocal laser scanning microscopy (CLSM) images (Fig. 3D), after 4 h of incubation, strong Sq fluorescence from FeS@BSA:Sq is observed in 4T1 cells, suggesting that FeS@BSA:Sq are able to enter 4T1 cells *via* endocytosis. Then, 4T1 cells were treated by FeS@BSA QDs plus laser irradiation, and the cell viability was calculated to be only 28% (Fig. 3E), which is significantly lower than the other three control groups (PBS incubation, laser irradiation only, and FeS@BSA incubation only). Therefore, FeS@BSA QDs are proven to be an efficient probe for PTT in cancer treatment.

3.4. In vivo T_1-weighted MR and PA imaging capability of FeS@BSA QDs

Based on the favorable *in vitro* results, we next investigated the T_1-weighted MR imaging capability of the synthesized FeS@BSA QDs in tumor-bearing mice, and the associated PA/fluorescence imaging capability were also assessed. Firstly, T_1-weighted MR/PA imaging were conducted before and after intravenous injection of FeS@BSA QDs (20 mg/kg, 150 μL) in 4T1 tumor-bearing mice. As depicted in Fig. 4A, FeS@BSA QDs can significantly light the tumor lesion in a gradient-enhanced manner. To be specific, the positive MR signal in tumor site is gradually enhanced within 5 h post-injection, and the signal is magnified by 1.8-fold at 5 h (Fig. 4B). The T_1-enhanced positive MR images suggest the synthesized biomimetic QDs are expectedly T_1 MR CAs which favors diagnostics for physicians, and particularly they can effectively accumulate at tumor sites for further treatment due to the enhanced penetration and retention (EPR) effect of nanomaterials and/or albumin-mediated tumor targeting [41,42].

Further leveraging the photo-thermal conversion capability of FeS@BSA QDs which was proved above, tumor was imaged under PA mode. Similar to T_1-weighted MR imaging results, the PA signal intensity was also found gradually enhanced over time post injection of FeS@BSA QDs (Fig. 4C). This result not only further suggests the time-dependent accumulation of FeS@BSA QDs in tumor region, but also shows the inherent bimodal imaging capability of the synthesized FeS@BSA QDs. Quantitatively, at 5 h post-injection, the average PA signal intensity of tumor is increased by 150% compared with pre-injection (Fig. 4D).

It should be noted that the tumor can be even visualized in this work by naked eyes after intravenous injection of the dark green FeS@BSA QDs. At 5 h post injection, the tumor lesion becomes dark like the colour of FeS@BSA QDs solution (Fig. 4E). This evidence clearly shows the strong tumor accumulation effect of FeS@BSA QDs. Similar results of high uptake of protein-mediated biomimetic nanoprobes by tumors have been shown in our previous work, which is most likely attributed to the unique features of the synthesized nanostructures, including ultrasmall size, highly water solubility, and endogenous protein coating [26]. To be detailed, the size is quite appropriate which is much smaller than that fabricated by conventional methods but slightly larger than that of small molecules. As a result, the probe with this favouring size has more opportunity to escape the liver uptake and circulate in bloodstream with a proper half-time but not rapidly excluded by kidneys. And the albumin protein layer on the nanoparticles is considered to block protein corona formation in body, acting as an invisible cloak to prolong half-life in circulation [24].

To investigate the biodistribution of FeS@BSA QDs in mice, a NIR dye, Sq, was loaded on the structure of FeS@BSA QDs *via* the hydrophobic domain of albumin, which is demonstrated in cell experiments. The integrated FeS@BSA:Sq was used to monitor *in vivo* biodistribution of FeS@BSA QDs by fluorescence imaging. Similarly, the fluorescence signal of tumor reaches maximum at 5 h post-injection, which is in accordance with MR/PA imaging results (Fig. 4F). Subsequently, the signal begins to decrease at 12 h and 24 h post injection (Fig. 4G). As presented in *ex vivo* fluorescence images of the major organs including heart, liver, spleen, lung, kidneys and the tumor before and at 5 h and 24 h post-injection (Fig. 4H), strong fluorescence signals in the liver, kidneys, and tumor were detected, which demonstrates the QDs undergo a liver and kidney combined clearance way. Therefore, by means of the complementary MR/PA/fluorescence imaging, the *in vivo* tumor accumulation and imaging capability of FeS@BSA QDs are clearly presented, and this imaging capability can guide the subsequent tumor therapy.

3.5. In vivo T_1-weighted MR imaging capability of FeS@BSA QDs in liver, kidneys, bladder and blood vessels

After confirming the T_1-weighted MR imaging capability of FeS@BSA QDs in tumor, we further evaluated its capability as T_1 MR CAs in

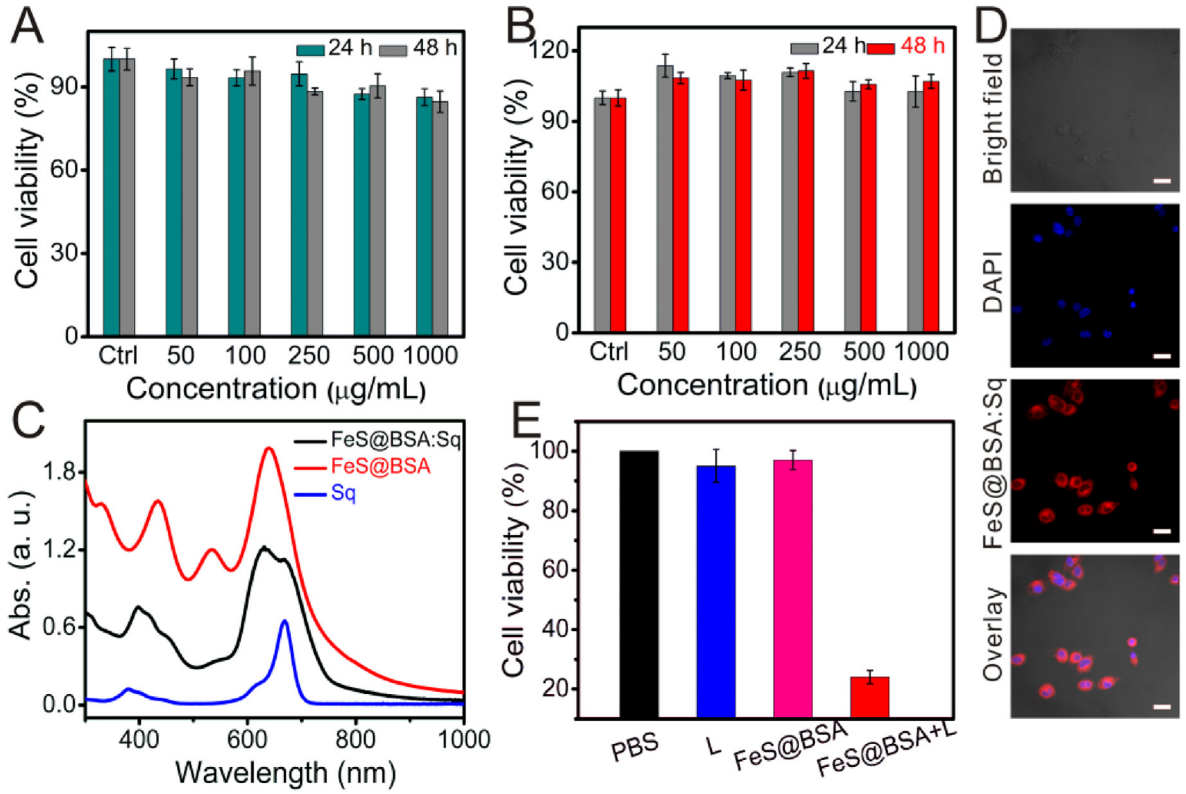

Fig. 3. *In vitro* cytotoxicity and laser-triggered phototherapy of breast cancer cells by using FeS@BSA QDs. The DC 2.4 (A) and 4T1 breast cancer cell (B) viability after incubation with different concentrations of FeS@BSA QDs (0–1000 μg/mL) for 24 h and 48 h, respectively; (C) The UV–vis absorption spectra of pure Sq, FeS@BSA, and FeS@BSA:Sq; (D) Confocal laser scanning microscope images of the 4T1 breast cancer cells after incubation with FeS@BSA:Sq for 4 h (Scale bar: 25 μm); . (E) The 4T1 breast cancer cell viability after different treatment, including control (PBS incubation), laser irradiation only (1 W/cm^2, 10 min), FeS@BSA incubation only (1 mg/mL), and FeS@BSA plus laser irradiation (1 W/cm^2, 10 min).

lighting the main metabolic organs, including liver, kidneys and bladder, and moreover the blood vessels. Thanks to the potent T_1-weighted MR imaging capability of FeS@BSA QDs, these main metabolic organs and the main blood vessels can be clearly visualized. Fig. 5A and B shows that the liver displays strong T_1 positive contrast enhancement after injection (2-fold at 3 h post-injection). We found the signals decreased at 5 h-post injection, indicating these QDs began metabolism. It should be noted that some iron-based nanoprobes can exhibit good T_1 signals *in vitro* but unfortunately they become T_2 MR CAs with negative enhancement behaviors in liver [43]. The main reason for this phenomenon is the aggregation of the swallowed nanoparticles in liver, which changes the magnetic property of iron nanoparticles. However, herein the albumin coating on FeS@BSA QDs can effectively inhibit or alleviate the aggregation effect, helping the FeS@BSA QDs maintain its T_1 magnetic environment. In addition, it can be seen from biodistribution of FeS@BSA QDs in main organs (determined by Fe content) that the spleen displayed a high uptake of FeS@BSA QDs at first 2 h and decreased subsequently (Fig. S10); and the tumor uptake at 6 h post-intravenous injection was significantly higher than that at 2 h due to the gradual accumulation of FeS@BSA QDs at tumor tissues during blood circulation. This high tumor uptake can guarantee the following therapy.

Then, we also found T_1 positive MR signal was increased in kidneys and bladder (Fig. 5A, C and D), demonstrating the renal clearance characteristic of FeS@BSA QDs due to the ultrasmall size that can be filtrated through the glomerulus to bladder [27,44]. Renal clearance is highly desired for imaging probes, which can reduce the toxicity of nanoparticles in liver [45].

In addition, we further evaluated the potential of our FeS@BSA QDs in T_1-weighted magnetic resonance angiography (MRA). MRA is frequently used in diagnosis of cardiovascular diseases; however, the specific CAs are still rare [46]. Fig. 5E shows MRA images of a mouse intravenously injected with FeS@BSA QDs. Due to the strong T_1 contrast and long circulation time, the blood vessels are clearly imaged. The corresponding MR signal intensity was measured to be nearly twice as high as pre-injection at the 5 min post-injection (Fig. 5F). Subsequently, as the reticuloendothelial (RES) system capture and the clearance continues, the T_1 signal in blood gradually decreases at 4 h post-injection. As shown in Fig. S11, the blood circulation half-life of FeS@BSA QDs was determined to be 2.12 h. Compared with the clinically-used small molecule MR CAs (like Gd (III) complexes), the time window of *in vivo* imaging is significantly prolonged from a few minutes to several hours, which allows sufficient time for diagnosis and subsequent treatment [24].

3.6. *In vivo* tumor PTT

In light of the good *in vitro* photothermal conversion effect of FeS@BSA QDs, tumor PTT was conducted in the 4T1-tumor bearing mice. As presented in the thermal images after laser irradiation (Fig. 6A), the tumor temperature with FeS@BSA QDs-treated mice rapidly increases from 26 °C to 57 °C, which is significantly higher than that of PBS-treated mice from 24 °C to 39 °C (Fig. 6B). The temperature of 57 °C is considered to be efficient to induce tumor ablation. Then, the tumor volume during treatment was monitored to reflect therapeutic efficacy. As depicted in Fig. 6C, the tumor growth of mice injected with FeS@BSA QDs plus laser irradiation are significantly suppressed at day 6 post-treatment. However, other mice treated with PBS only, laser irradiation only, and FeS@BSA QDs only grow rapidly. Moreover, the body weights of mice were found to be slightly increased but without significantly difference between groups (Fig. 6D), suggesting no obvious side effects of PTT treatment in our study. Both the representative

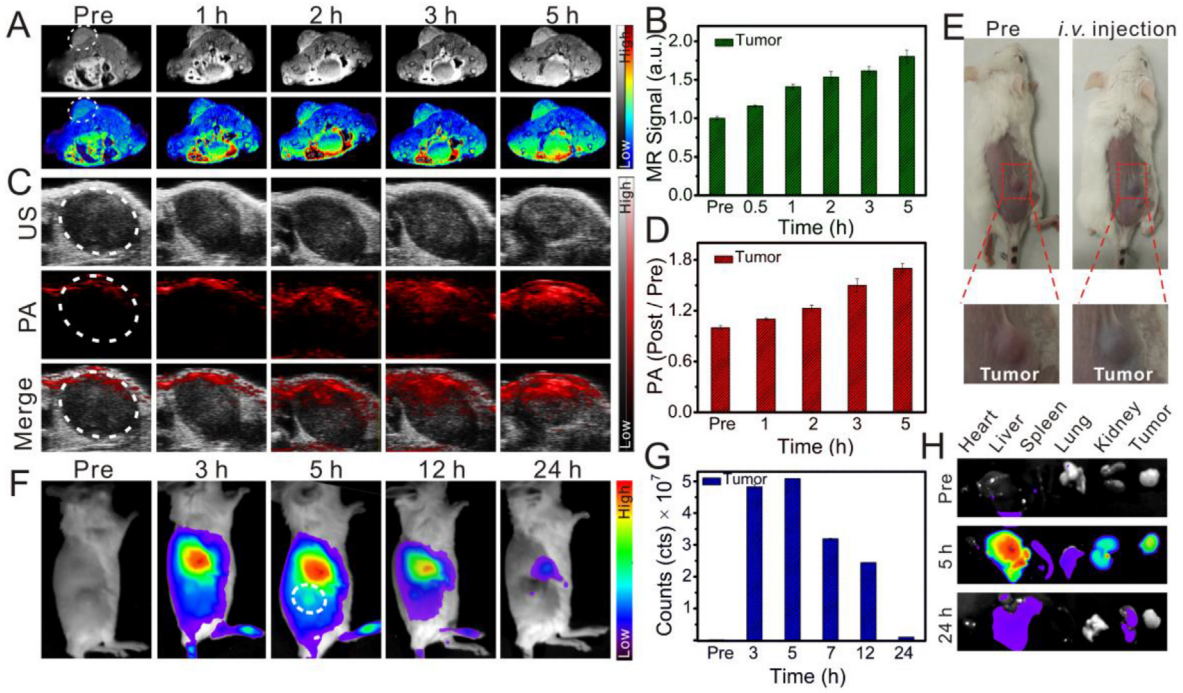

Fig. 4. *In vivo* T_1-weighted MR and PA imaging and biodistribution of FeS@BSA QDs in tumor-bearing mice. (A) Time-dependent T_1-weighted MR images of tumor and (B) the corresponding MR signal intensity before and after intravenous injection of FeS@BSA QDs (20 mg/kg); (C) The US, PA, and merged (US + PA) images of tumor and (D) corresponding PA signal intensity of pre-/post-injection at different time points; (E) The digital photos of mouse before and after intravenous injection of FeS@BSA QDs. The red box indicates the tumor site; (F) The fluorescence images of mice before and after intravenous injection of FeS@BSA:Sq QDs; (G) The fluorescence signal intensity of tumor at different time points; (H) The main organs (S: Spleen H: Heart, L: Lung, K: Kidney, L: Liver) distribution containing FeS@BSA:Sq QDs at 5 h and 24 h post-injection. The white doted circle in F indicates the tumour site. (For interpretation of the references to colour in this figure legend, the reader is referred to the Web version of this article.)

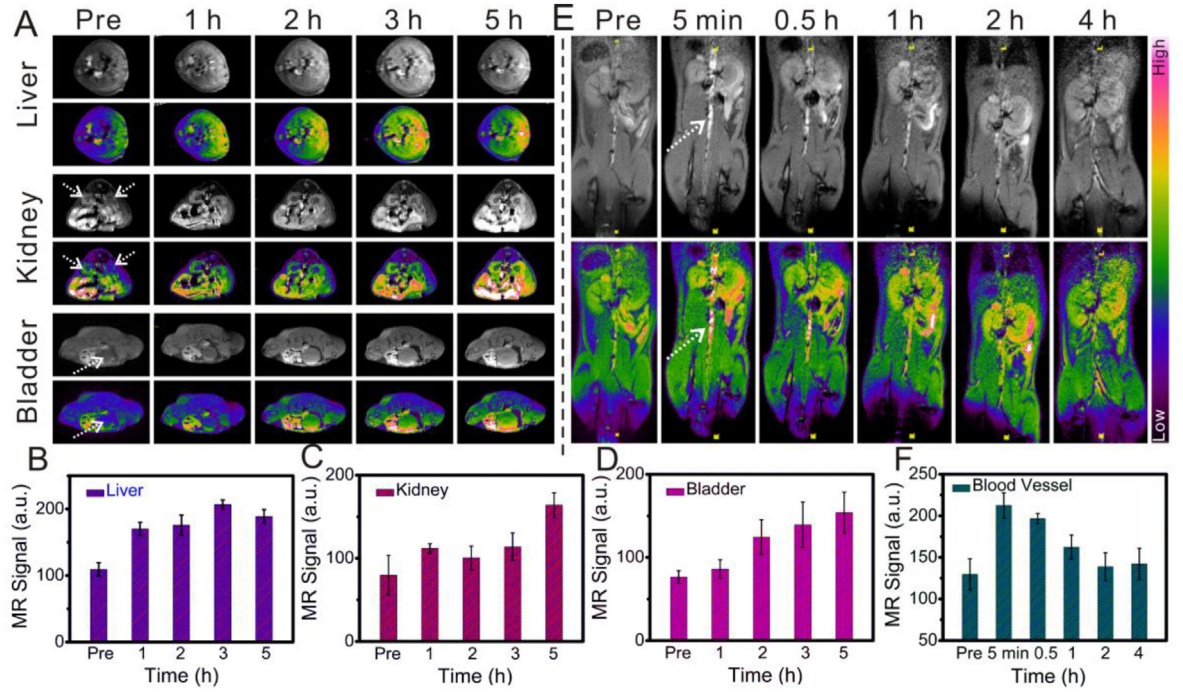

Fig. 5. T_1-weighted MR imaging capability of FeS@BSA QDs in metabolic organs and the blood vessels. (A) Time-dependent T_1-weighted MR images of liver, kidney, bladder, and the corresponding MR signal intensity ((B), liver; (C), kidney; (D), bladder) before and after intravenous injection of FeS@BSA QDs (20 mg/kg) at different time points (1 h, 2 h, 3 h, and 5 h); (E) T_1-weighted blood-pool MR images and (F) the corresponding signal intensity of mice before and post-intravenous injection by FeS@BSA QDs at different time points. The white dotted arrows in (A) and (E) indicate the kidney, bladder, and blood vessel, respectively.

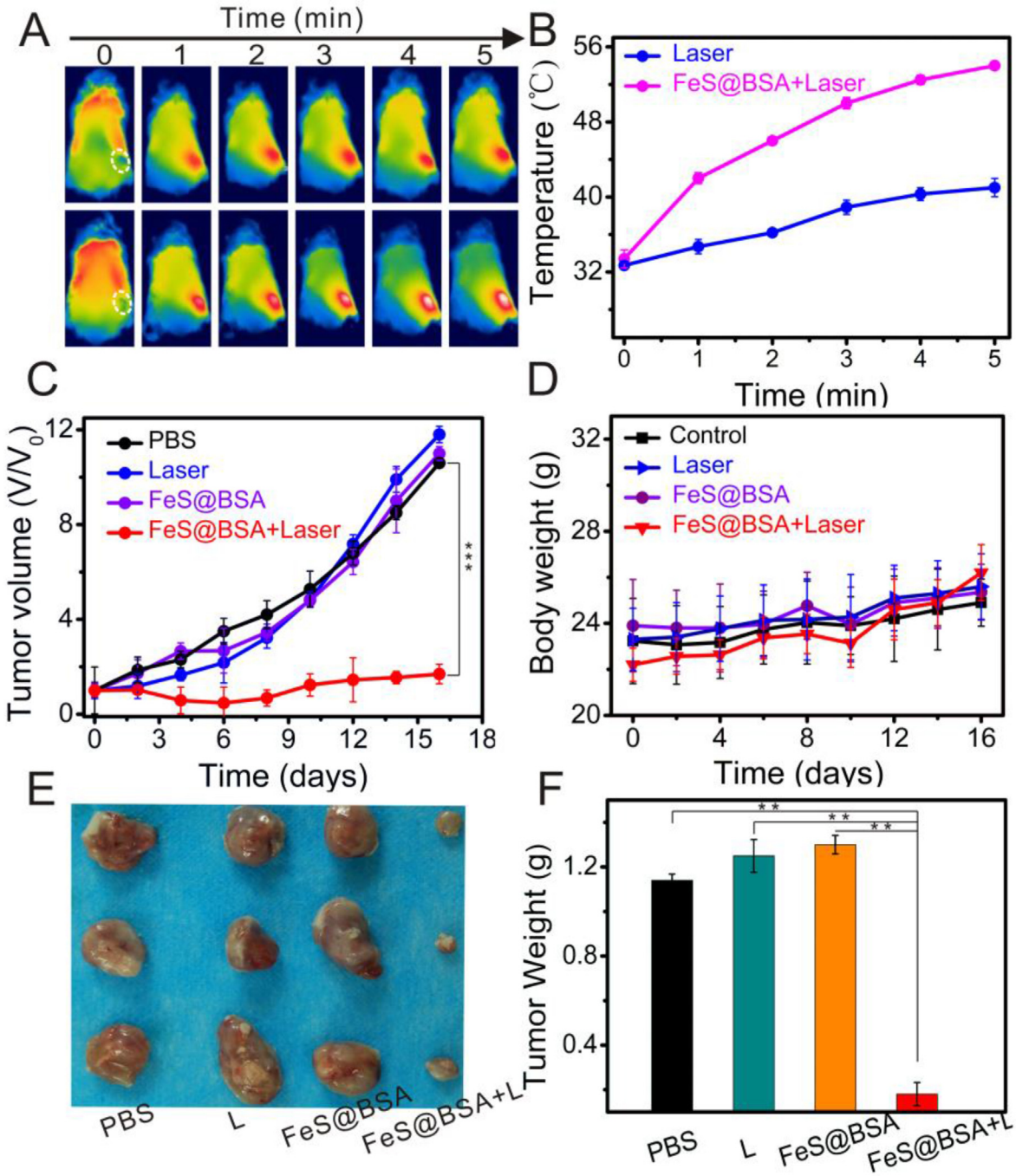

Fig. 6. *In vivo* tumor PTT. (A) Photothermal images of 4T1 tumor-bearing mice injected with PBS plus laser irradiation and FeS@BSA QDs plus laser irradiation, respectively. (B) The temperature growth curve during 5 min of laser irradiation. (C) Relative tumor volume changes of mice in four groups (PBS injection, laser irradiation, FeS@BSA QDs injection, and FeS@BSA QDs injection plus laser irradiation) over 16 days; (D) Average body weight of mice from different treatment groups; (E) Photos and (F) average weight of the excised tumors from mice on the day 16 after different treatments (**p < 0.01, ***P < 0.001).

images (Fig. 6E) and average weight (Fig. 6F) of the dissected tumor show that the tumors of mice treated with FeS@BSA QDs plus laser irradiation are much smaller than the other three groups, confirming the good performance of PTT by the synthesized FeS@BSA QDs.

To further present the PTT efficacy of FeS@BSA QDs, tumors from different groups were sliced and stained with H&E for histological analysis (Fig. S12). Notably, the tumor treated by FeS@BSA QDs plus laser irradiation shows sign of cell necrosis, while the tissue structures of the other three groups (control, laser irradiation only, and FeS@BSA QDs treatment only) are almost intact. These data collectively disclose the good PTT effect of FeS@BSA QDs, besides their imaging capability.

3.7. *In vivo* toxicology assessment of FeS@BSA QDs

To evaluate the *in vivo* biosafety of FeS@BSA QDs, biochemical and blood routine tests of mice before and after intravenous injection of FeS@BSA QDs were conducted. As shown in Fig. 7A–D, biochemical test results demonstrate no significant difference in the levels of liver function markers (AST, ALP, ALT, ALB, A/G) and kidney function markers (UREA) compared to the control group, which indicates no/low hepatic or kidney dysfunction induced by FeS@BSA QDs at the investigated concentration. Moreover, eight key blood routine markers, including red blood cells (RBC), mean corpuscular hemoglobin (MCH),

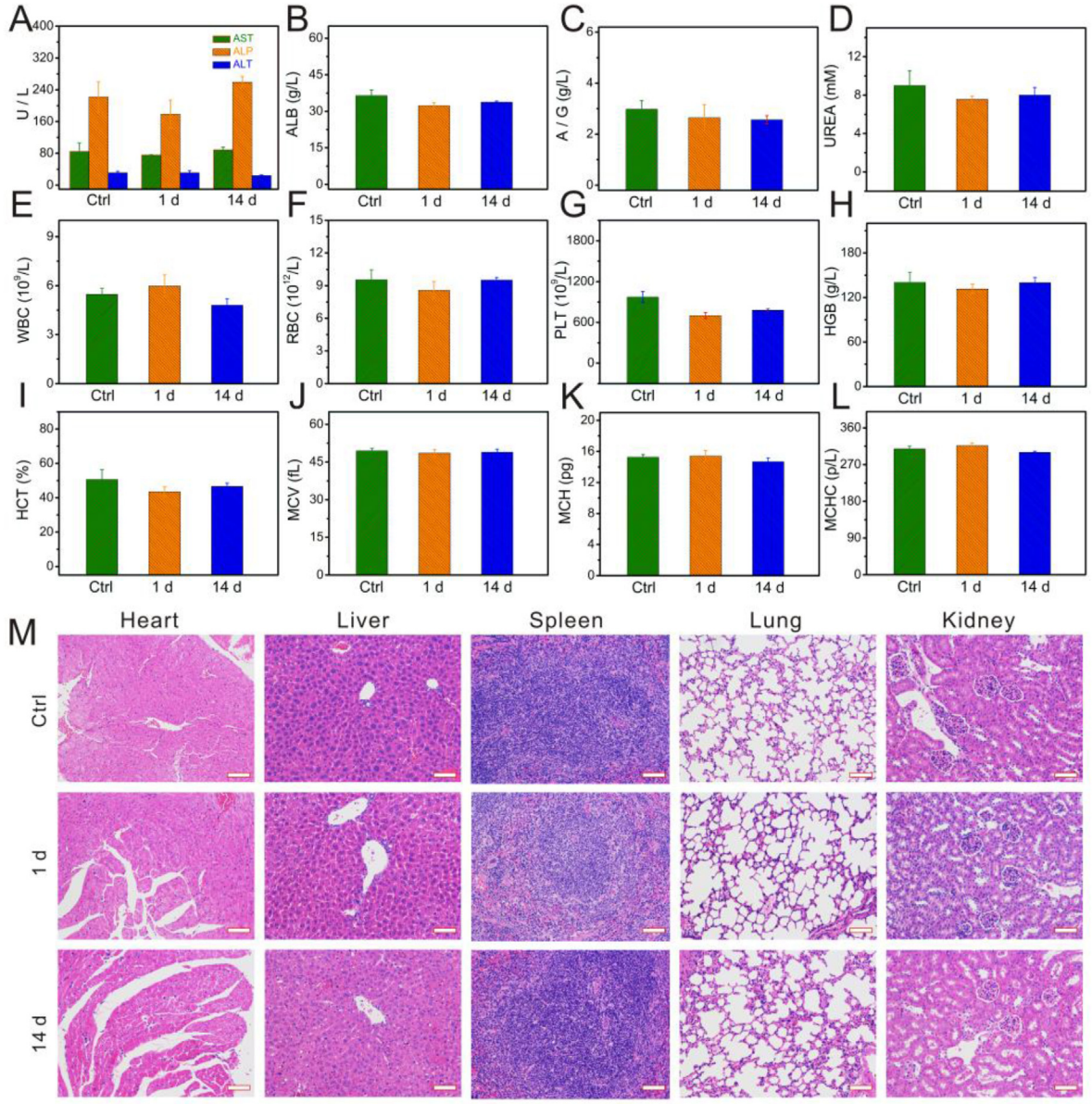

Fig. 7. *In vivo* biosafety evaluation of FeS@BSA QDs. (A)–(D) Biochemical tests and (E)–(L) blood routine tests based on blood samples collected from mice pre and post intravenous injection of FeS@BSA QDs (day 1 and day 14), including liver functions ((A) ALT, AST, ALP, (B) ALB, (C) A/G), renal function (D) UREA), and eight key blood routine indicators (E) WBC, (F) RBC, (G) PLT, H) HGB, (I) HCT, (J) MCV, (K), MCH, (L) MCHC. Values are presented as means ± s. d. (n = 3); M) H&E-staining of organ tissues from the mice before and after intravenous injection of FeS@BSA QDs (day 1 and day 14). Scale bar: 50 μm.

hemoglobin (HGB), hematocrit (HCT), platelets (PLT), mean corpuscular hemoglobin concentration (MCHC), white blood cells (WBC), mean corpuscular volume (MCV), were measured for systematically evaluating the hemocompatibility. As displayed in Fig. 7E–L, these marker values are within the normal range and show no observable variations, indicating good blood compatibility of FeS@BSA QDs in the investigated concentration.

In addition, H&E staining examination of major organs (liver, kidney, lung, heart, and spleen) was conducted before and at day 1 and day 14 post injection of FeS@BSA QDs (20 mg/kg mice). As presented in Fig. 7M, the tissue structures of the mice at day 1 and day 14 post-injection of FeS@BSA QDs are intact, and no obvious pathological changes, such as organ damage, inflammatory lesions, and cell necrosis are observed. It should be noted that FeS@BSA QDs can be used for Fenton reaction for tumor therapy since they contained iron element. Certainly, in this study for imaging use, the dose of FeS@BSA QDs should be controlled to avoid the toxicity caused by Fenton chemistry.

4. Conclusions

In summary, this work demonstrates albumin-constrained biomimetic synthesis of ultrasmall FeS@BSA QDs for T_1-weighted MR imaging of tumor, metabolic organs and blood vessels. This synthetic strategy was found green, concise, and efficient. And particularly the synthesis of FeS@BSA QDs is large-scalable and reproducible. The obtained FeS@BSA QDs delimited by protein are ultrasmall in size of *ca.* 3 nm with a very low magnetization and thus exhibit a much higher longitudinal relaxation rate than that of their large-sized counterparts and even the clinically-used Gd-DTPA. And interestingly, FeS@BSA QDs have good photo-thermal conversion capability, therefore enabling them to be an efficient T_1-weighted MR/PA/PTT theranostic agent. *In vivo* tumor-bearing mice experiments show good performance of FeS@BSA QDs in tumor targeting enhancement under the T_1-weighted MR imaging/PA modalities. Besides tumor imaging, FeS@BSA QDs also exhibit pretty good T_1-weighted MR imaging quality in lighting the

liver, kidneys and bladder, and even the blood vessels. And importantly, these QDs can be finally cleared from body *via* urine after theranostics.

To the best of our knowledge, our study provides the first demonstration of using albumin on constrained-synthesis of ultrasmall iron-based nanoparticles to improve its longitudinal relaxation rate for T_1-weighted MR imaging and serendipitously endowed with PA imaging and PTT therapy capabilities. Given this design does not require any complicated chemical synthesis or modification, and the synthetic process including the raw materials are bioinspired, environmentally benign, and straightforward, the method demonstrated in this work will find wide applications for fabricating advanced nanoprobes for imaging and therapy of diseases.

CRediT authorship contribution statement

Weitao Yang: Conceptualization, Methodology, Software, Writing - review & editing. **Chenyang Xiang:** Data curation, Writing - original draft. **Yan Xu:** Software. **Shizhen Chen:** Investigation. **Weiwei Zeng:** Visualization. **Kai Liu:** Validation. **Xiao Jin:** Investigation. **Xin Zhou:** Supervision. **Bingbo Zhang:** Conceptualization, Methodology, Software, Writing - review & editing.

Declaration of competing interest

The authors declare no conflict of interest.

Acknowledgments

This work was funded by the National Natural Science Foundation of China (81871399, 81625011, 81801823, 91859206, 81922035), State Key Laboratory of Molecular Engineering of Polymers (Fudan University, K2020-16), the Research Fund from State Key Laboratory of Magnetic Resonance and Atomic and Molecular Physics, Wuhan Institute of Physics and Mathematics, CAS (T151701), National Key R& D Program of China (2018YFA0704000), Shanghai Science and Technology Biomedical Innovation Funds (19441904200), and Young Hundred-Talent Program of Tongji University.

Appendix A. Supplementary data

Supplementary data to this article can be found online at https://doi.org/10.1016/j.biomaterials.2020.120186.

References

[1] Y. Zhao, J. Peng, J. Li, L. Huang, J. Yang, K. Huang, H. Li, N. Jiang, S. Zheng, X. Zhang, Tumor-targeted and clearable human protein-based MRI nanoprobes, Nano Lett. 17 (2017) 4096–4100.
[2] P. Mi, D. Kokuryo, H. Cabral, H. Wu, Y. Terada, T. Saga, I. Aoki, N. Nishiyama, K. Kataoka, A pH-activatable nanoparticle with signal-amplification capabilities for non-invasive imaging of tumour malignancy, Nat. Nanotechnol. 11 (2016) 724.
[3] X. Hu, G. Liu, Y. Li, X. Wang, S. Liu, Cell-penetrating hyperbranched polyprodrug amphiphiles for synergistic reductive milieu-triggered drug release and enhanced magnetic resonance signals, J. Am. Chem. Soc. 137 (2015) 362–368.
[4] W.A. Willinek, H.H. Schild, Clinical advantages of 3.0 T MRI over 1.5 T, Eur. J. Radiol. 65 (2008) 2–14.
[5] R.J. Holbrook, N. Rammohan, M.W. Rotz, K.W. MacRenaris, A.T. Preslar, T.J. Meade, Gd (III)-dithiolane gold nanoparticles for T_1-weighted magnetic resonance imaging of the pancreas, Nano Lett. 16 (2016) 3202–3209.
[6] F. Li, Z. Liang, J. Liu, J. Sun, X. Hu, M. Zhao, J. Liu, R. Bai, D. Kim, X. Sun, Dynamically reversible iron oxide nanoparticle assemblies for targeted amplification of T1-weighted magnetic resonance imaging of tumors, Nano Lett. 19 (2019) 4213–4220.
[7] D. Ni, J. Zhang, J. Wang, P. Hu, Y. Jin, Z. Tang, Z. Yao, W. Bu, J. Shi, Oxygen vacancy enables markedly enhanced magnetic resonance imaging-guided photothermal therapy of a Gd^{3+}-doped contrast agent, ACS Nano 11 (2017) 4256–4264.
[8] J. Wahsner, E.M. Gale, A. Rodríguez-Rodríguez, P. Caravan, Chemistry of MRI contrast agents: current challenges and new frontiers, Chem. Rev. 119 (2018) 957–1057.
[9] J. Lin, M. Wang, H. Hu, X. Yang, B. Wen, Z. Wang, O. Jacobson, J. Song, G. Zhang, G. Niu, Multimodal-imaging-guided cancer phototherapy by versatile biomimetic theranostics with UV and γ-irradiation protection, Adv. Mater. 28 (2016) 3273–3279.
[10] C. Tassa, S.Y. Shaw, R. Weissleder, Dextran-coated iron oxide nanoparticles: a versatile platform for targeted molecular imaging, molecular diagnostics, and therapy, Acc. Chem. Res. 44 (2011) 842–852.
[11] D. Ni, W. Bu, E.B. Ehlerding, W. Cai, J. Shi, Engineering of inorganic nanoparticles as magnetic resonance imaging contrast agents, Chem. Soc. Rev. 46 (2017) 7438–7468.
[12] U.I. Tromsdorf, O.T. Bruns, S.C. Salmen, U. Beisiegel, H. Weller, A highly effective, nontoxic T_1 MR contrast agent based on ultrasmall PEGylated iron oxide nanoparticles, Nano Lett. 9 (2009) 4434–4440.
[13] B.H. Kim, N. Lee, H. Kim, K. An, Y.I. Park, Y. Choi, K. Shin, Y. Lee, S.G. Kwon, H.B. Na, Large-scale synthesis of uniform and extremely small-sized iron oxide nanoparticles for high-resolution T_1 magnetic resonance imaging contrast agents, J. Am. Chem. Soc. 133 (2011) 12624–12631.
[14] Z. Zhou, L. Wang, X. Chi, J. Bao, L. Yang, W. Zhao, Z. Chen, X. Wang, X. Chen, J. Gao, Engineered iron-oxide-based nanoparticles as enhanced T_1 contrast agents for efficient tumor imaging, ACS Nano 7 (2013) 3287–3296.
[15] H. Zhang, L. Li, X.L. Liu, J. Jiao, C.-T. Ng, J.B. Yi, Y.E. Luo, B.-H. Bay, L.Y. Zhao, M.L. Peng, Ultrasmall ferrite nanoparticles synthesized via dynamic simultaneous thermal decomposition for high-performance and multifunctional T_1 magnetic resonance imaging contrast agent, ACS Nano 11 (2017) 3614–3631.
[16] Q. Weng, X. Hu, J. Zheng, F. Xia, N. Wang, H. Liao, Y. Liu, D. Kim, J. Liu, F. Li, Toxicological risk assessments of iron oxide nanocluster-and gadolinium-based T_1 MRI Contrast Agents in Renal Failure Rats, ACS Nano 13 (2019) 6801–6812.
[17] Y. Lu, Y.-J. Xu, G.-b. Zhang, D. Ling, M.-q. Wang, Y. Zhou, Y.-D. Wu, T. Wu, M.J. Hackett, B.H. Kim, Iron oxide nanoclusters for T_1 magnetic resonance imaging of non-human primates, Nat. Biomed. Eng. 1 (2017) 637.
[18] Z. Meng, F. Wei, W. Ma, N. Yu, P. Wei, Z. Wang, Y. Tang, Z. Chen, H. Wang, M. Zhu, Design and synthesis of "All-in-One" multifunctional FeS_2 nanoparticles for magnetic resonance and near-infrared imaging guided photothermal therapy of tumors, Adv. Funct. Mater. 26 (2016) 8231–8242.
[19] J. Park, K. An, Y. Hwang, J.-G. Park, H.-J. Noh, J.-Y. Kim, J.-H. Park, N.-M. Hwang, T. Hyeon, Ultra-large-scale syntheses of monodisperse nanocrystals, Nat. Mater. 3 (2004) 891.
[20] L.-h. Shen, J.-f. Bao, D. Wang, Y.-x. Wang, Z.-w. Chen, L. Ren, X. Zhou, X.-b. Ke, M. Chen, A.-q. Yang, One-step synthesis of monodisperse, water-soluble ultra-small Fe_3O_4 nanoparticles for potential bio-application, Nanoscale 5 (2013) 2133–2141.
[21] C. Wadia, Y. Wu, S. Gul, S.K. Volkman, J. Guo, A.P. Alivisatos, Surfactant-assisted hydrothermal synthesis of single phase pyrite FeS_2 nanocrystals, Chem. Mater. 21 (2009) 2568–2570.
[22] Z. Wang, P. Huang, O. Jacobson, Z. Wang, Y. Liu, L. Lin, J. Lin, N. Lu, H. Zhang, R. Tian, G. Niu, G. Liu, X. Chen, Biomineralization-inspired synthesis of copper sulfide-ferritin nanocages as cancer theranostics, ACS Nano 10 (2016) 3453–3460.
[23] W. Yang, W. Guo, W. Le, G. Lv, F. Zhang, L. Shi, X. Wang, J. Wang, S. Wang, J. Chang, Albumin-bioinspired Gd: CuS nanotheranostic agent for in vivo photoacoustic/magnetic resonance imaging-guided tumor-targeted photothermal therapy, ACS Nano 10 (2016) 10245–10257.
[24] B. Zhang, H. Jin, Y. Li, B. Chen, S. Liu, D. Shi, Bioinspired synthesis of gadolinium-based hybrid nanoparticles as MRI blood pool contrast agents with high relaxivity, J. Mater. Chem. 22 (2012) 14494–14501.
[25] J. Zhang, G. Hao, C. Yao, J. Yu, J. Wang, W. Yang, C. Hu, B. Zhang, Albumin-mediated biomineralization of paramagnetic NIR Ag_2S QDs for tiny tumor bimodal targeted imaging *in vivo*, ACS Appl. Mater. Interfaces 8 (2016) 16612–16621.
[26] W. Yang, X. Wu, Y. Dou, J. Chang, C. Xiang, J. Yu, J. Wang, X. Wang, B. Zhang, A human endogenous protein exerts multi-role biomimetic chemistry in synthesis of paramagnetic gold nanostructures for tumor bimodal imaging, Biomaterials 161 (2018) 256–269.
[27] J. Wang, G. Liu, Imaging nano-bio interactions in the kidney: toward a better understanding of nanoparticle clearance, Angew. Chem. Int. Ed. 57 (2018) 3008–3010.
[28] J. Hu, L.-s. Li, W. Yang, L. Manna, L.-w. Wang, A.P. Alivisatos, Linearly polarized emission from colloidal semiconductor quantum rods, Science 292 (2001) 2060–2063.
[29] Y. Liu, W. Xiao, J. Wang, Z.A. Mirza, T. Wang, Optimized synthesis of FeS nanoparticles with a high Cr (VI) removal capability, J. Nanomater. 2016 (2016) 48.
[30] B. Crist, BE Lookup Table for Signals from Elements and Common Chemical Species, Wiley, Chichester, UK, 1999, pp. 77–358.
[31] Z. Tang, H. Zhang, Y. Liu, D. Ni, H. Zhang, J. Zhang, Z. Yao, M. He, J. Shi, W. Bu, Antiferromagnetic pyrite as the tumor microenvironment-mediated nanoplatform for self-enhanced tumor imaging and therapy, Adv. Mater. 29 (2017) 1701683.
[32] H. Chen, Y. Qiu, D. Ding, H. Lin, W. Sun, G.D. Wang, W. Huang, W. Zhang, D. Lee, G. Liu, Gadolinium-encapsulated graphene carbon nanotheranostics for imaging-guided photodynamic therapy, Adv. Mater. 30 (2018) 1802748.
[33] F. Liu, X. He, H. Chen, J. Zhang, H. Zhang, Z. Wang, Gram-scale synthesis of coordination polymer nanodots with renal clearance properties for cancer theranostic applications, Nat. Commun. 6 (2015) 8003.
[34] J.-s. Choi, S. Kim, D. Yoo, T.-H. Shin, H. Kim, M.D. Gomes, S.H. Kim, A. Pines, J. Cheon, Distance-dependent magnetic resonance tuning as a versatile MRI sensing platform for biological targets, Nat. Mater. 16 (2017) 537.
[35] X.Y. Zheng, K. Zhao, J. Tang, X.Y. Wang, L.D. Li, N.X. Chen, Y.J. Wang, S. Shi, X. Zhang, S. Malaisamy, Gd-dots with strong ligand–water interaction for ultra-sensitive magnetic resonance renography, ACS Nano 11 (2017) 3642–3650.
[36] X. Cai, W. Gao, M. Ma, M. Wu, L. Zhang, Y. Zheng, H. Chen, J. Shi, A prussian blue-based core-shell hollow-structured mesoporous nanoparticle as a smart

theranostic agent with ultrahigh pH-responsive longitudinal relaxivity, Adv. Mater. 27 (2015) 6536.
[37] E.J. Werner, A. Datta, C.J. Jocher, K.N. Raymond, High-relaxivity MRI contrast agents: where coordination chemistry meets medical imaging, Angew. Chem. Int. Ed. 47 (2008) 8568–8580.
[38] L. Wang, X. Zhu, X. Tang, C. Wu, Z. Zhou, C. Sun, S.-L. Deng, H. Ai, J. Gao, A multiple gadolinium complex decorated fullerene as a highly sensitive T_1 contrast agent, Chem. Commun. 51 (2015) 4390–4393.
[39] D.K. Roper, W. Ahn, M. Hoepfner, Microscale heat transfer transduced by surface plasmon resonant gold nanoparticles, J. Phys. Chem. C 111 (2007) 3636–3641.
[40] X. Guo, B. Cao, C. Wang, S. Lu, X. Hu, In vivo photothermal inhibition of methicillin-resistant Staphylococcus aureus infection by in situ templated formulation of pathogen-targeting phototheranostics, Nanoscale 12 (14) (2020) 7651–7659.
[41] T. Lin, P. Zhao, Y. Jiang, Y. Tang, H. Jin, Z. Pan, H. He, V.C. Yang, Y. Huang, Blood–brain-barrier-penetrating albumin nanoparticles for biomimetic drug delivery via albumin-binding protein pathways for antiglioma therapy, ACS Nano 10 (2016) 9999–10012.
[42] X. Wan, H. Zhong, W. Pan, Y. Li, Y. Chen, N. Li, B. Tang, Programmed release of dihydroartemisinin for synergistic cancer therapy using a $CaCO_3$ mineralized metal–organic framework, Angew. Chem. Int. Ed. 131 (2019) 14272–14277.
[43] L. Dai, Y. Liu, Z. Wang, F. Guo, D. Shi, B. Zhang, One-pot facile synthesis of PEGylated superparamagnetic iron oxide nanoparticles for MRI contrast enhancement, Mater. Sci. Eng. C-Mater. 41 (2014) 161–167.
[44] B. Du, X. Jiang, A. Das, Q. Zhou, M. Yu, R. Jin, J. Zheng, Glomerular barrier behaves as an atomically precise bandpass filter in a sub-nanometre regime, Nat. Nanotechnol. 12 (2017) 1096.
[45] H. Wang, D. Yu, J. Fang, C. Cao, Z. Liu, J. Ren, X. Qu, Renal-clearable porphyrinic metal–organic framework nanodots for enhanced photodynamic therapy, ACS Nano 13 (2019) 9206–9217.
[46] H. Wei, O.T. Bruns, M.G. Kaul, E.C. Hansen, M. Barch, A. Wiśniowska, O. Chen, Y. Chen, N. Li, S. Okada, Exceedingly small iron oxide nanoparticles as positive MRI contrast agents, P. Natl. Acad. Sci. USA. 114 (2017) 2325–2330.